AGU PUBLICATIONS

Geochemistry, Geophysics, Geosystems

RESEARCH ARTICLE
10.1002/2014GC005581

Key Points:
- The Moho is weak below the arc
- No mafic-ultramafic crust is imaged
- Slow mantle at 70 km depth indicates melt

Supporting Information:
- Readme
- FigureSI1mapevents
- FigureSI2fitdata1
- FigureSI2fitdata2
- FigureSI2fitdata3
- FigureSI3geotherms

Correspondence to:
M. Obrebski,
obrebski.mathias@gmail.com

Citation:
Obrebski, M., G. A. Abers, and A. Foster (2015), Magmatic arc structure around Mount Rainier, WA, from the joint inversion of receiver functions and surface wave dispersion, *Geochem. Geophys. Geosyst.*, *16*, 178–194, doi:10.1002/2014GC005581.

Received 19 SEP 2014
Accepted 29 NOV 2014
Accepted article online 4 DEC 2014
Published online 22 JAN 2015

Magmatic arc structure around Mount Rainier, WA, from the joint inversion of receiver functions and surface wave dispersion

Mathias Obrebski[1,4], Geoffrey A. Abers[2], and Anna Foster[3]

[1]Lamont-Doherty Earth Observatory of Columbia University, Palisades, New York, USA, [2]Department of Earth and Atmospheric Sciences, Cornell University, Ithaca, New York, USA, [3]Earth Observatory of Singapore, Nanyang Technological University, Singapore, Singapore, [4]División Ciencias de la Tierra, Centro de Investigación Científica y de Educación Superior de Ensenada, Ensenada, Baja California, Mexico

Abstract The deep magmatic processes in volcanic arcs are often poorly understood. We analyze the shear wave velocity (V_S) distribution in the crust and uppermost mantle below Mount Rainier, in the Cascades arc, resolving the main velocity contrasts based on converted phases within P coda via source normalization or receiver function (RF) analysis. To alleviate the trade-off between depth and velocity, we use long period phase velocities (25–100 s) obtained from earthquake surface waves, and at shorter period (7–21 s) we use seismic noise cross correlograms. We use a transdimensional Bayesian scheme to explore the model space (V_S in each layer, number of interfaces and their respective depths, level of noise on data). We apply this tool to 15 broadband stations from permanent and Earthscope temporary stations. Most results fall into two groups with distinctive properties. Stations east of the arc (Group I) have comparatively slower middle-to-lower crust (V_S = 3.4–3.8 km/s at 25 km depth), a sharp Moho and faster uppermost mantle (V_S = 4.2–4.4 km/s). Stations in the arc (Group II) have a faster lower crust (V_S = 3.7–4 km/s) overlying a slower uppermost mantle (V_S = 4.0–4.3 km/s), yielding a weak Moho. Lower crustal velocities east of the arc (Group I) most likely represent ancient subduction mélanges mapped nearby. The lower crust for Group II ranges from intermediate to felsic. We propose that intermediate-felsic to felsic rocks represent the prearc basement, while intermediate composition indicates the mushy andesitic crustal magmatic system plus solidified intrusion along the volcanic conduits. We interpret the slow upper mantle as partial melt.

1. Introduction

Magmatic processes along active arcs, from melting in the wedge to the storage, chemical differentiation, and eruption or settlement of magmatic bodies, are still poorly understood. The deployments of seismic arrays around active volcanoes have provided short-period data that illuminate the upper crustal structure of many active volcanoes [*Brenguier et al.*, 2007; *Lees*, 2007; *Okubo et al.*, 1997]. The structure of the lower crust and uppermost mantle is less documented, but is critical to many models of arc magmatic differentiation and growth [*Annen et al.*, 2006; *Behn and Kelemen*, 2006; *Tatsumi et al.*, 2008]. The repeated transfer of magma and heat from the mantle to the crust is thought to generate piles of dense mafic cumulates and restites that can significantly modify the composition of the lower crust, which together with in situ magma can blur the seismic signature of the Mohorovičić discontinuity ("Moho"), and possibly trigger gravitational foundering of lower arc crust [*Jull and Kelemen*, 2001; *Kay and Kay*, 1993]. The extent to which magma remains in situ within the lower crust and uppermost mantle in magma chambers and mush zones is also poorly known, and some evidence suggests very rapid transport from mantle depths to the surface [*Ruprecht and Plank*, 2013].

The purpose of the current analysis is to put tighter constraints on the seismic structure of the crust and uppermost mantle below and in the immediate vicinity of Mount Rainier, with the ultimate objective of understanding how arc magmatism alters the crust. We take advantage of the recent deployment of the Cascadia Arrays For Earthscope (CAFE) [*Abers et al.*, 2009] and combine this data set with the Bayesian approach developed by *Bodin et al.* [2012] to jointly invert receiver functions (RFs) and phase velocity constraints obtained from ambient noise correlation [*Calkins et al.*, 2011] and teleseismic surface wave measurements [*Foster et al.*, 2014]. Receiver functions constrain velocity contrasts while surface waves are sensitive

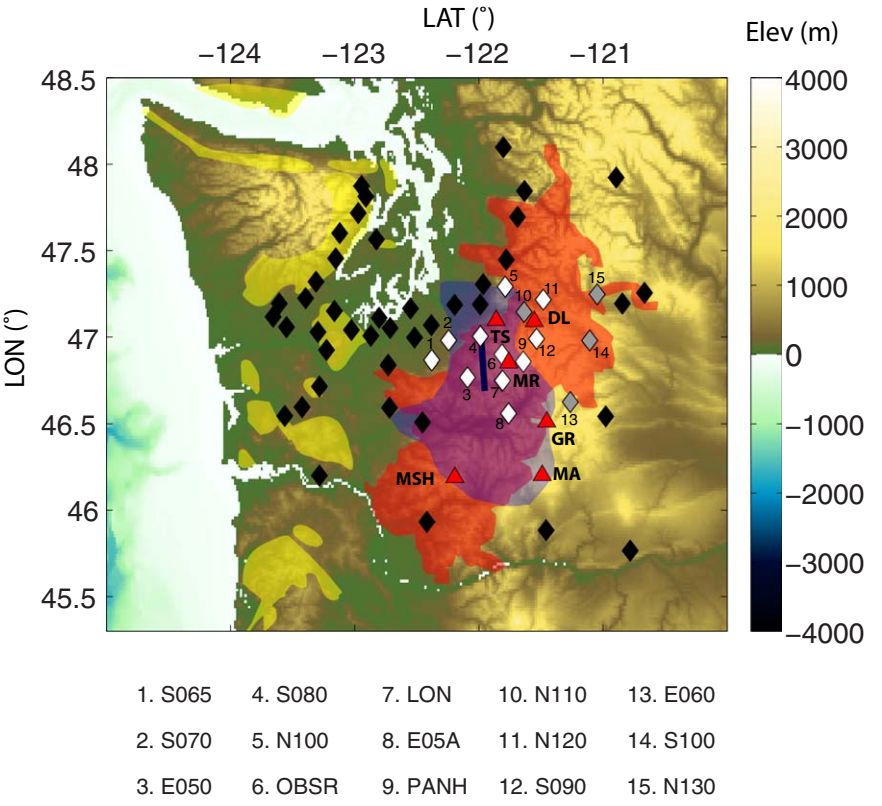

Figure 1. Physiographic map of the Cascades around Mount Rainier and station distribution. The red and yellow shaded areas show the Ancestral Cascades and outcrop of the Siletzia Terrane. The thick black line shows the West Rainier Seismic Zone (WRSZ). The blue shaded area shows the Southern Washington Crustal Conductor (SWCC). Diamonds indicate the stations used here; white: Group II, gray: Group I; black: used in ambient-noise correlation measurements but not for joint inversions. The red triangles are Quaternary volcanic centers: MSH, Mount Saint Helens; GR, Goat Rocks; MR, Mount Rainier; MA, Mount Adams; TS, Three Sisters vents; and DL, Dalles Lakes vents.

to vertical averages of seismic velocity. The combination of both types of constraints alleviates the trade-off between depth and velocity intrinsic to both types of analysis individually. We first present the data set and methodology, and then describe the resulting velocity models and how they compare with previous studies. Finally, we use these results to discuss the structure, physical state, and composition of the crust and mantle wedge.

2. Cascadia Regional Setting

Magmatism in the Washington Cascades initiated in the Eocene and migrated eastward to its current location, dividing the arc into two domains: the western or Ancestral Cascades arc active between 45 and 4 Ma, and the High Cascades with onset at 10 Ma (Figure 1). Modern arc magmatism results from the subduction of the young Juan de Fuca plate. The arc formed on the crust of the Columbia Embayment, a province thought to be of oceanic origin [*Miller*, 1989] and characterized by distinctive magnetic and gravimetric signatures [*Couch and Riddihough*, 1989; *Finn*, 1990]. The largest block is the Siletzia Terrane, an oceanic plateau that outcrops along the Coast Ranges and has been seismically imaged to be at 10–15 km depth in southwestern Washington [*Parsons et al*., 1999]. The exact location of its eastern edge is still debated. Some authors proposed it is buried west of Mount Rainier [*Parsons et al*., 1999] and coincides with the Western Rainier Seismic Zone (Figure 1). However, *Gao et al*. [2011] propose that the Siletzia crust extends much further east, where at depth fossil subducted slab is seismically imaged close to the Washington-Idaho-Oregon border [*Schmandt and Humphreys*, 2011].

The main target of this study is Mount Rainier, a stratovolcano located at a transition between widespread diffuse mafic magmatism to the south and negligible mafic volcanism to the north [*Schmidt et al*., 2008]. Mount Rainier axial products are mostly calc-alkaline andesite, and dacite to a lesser extent [*Hildreth*, 2007;

Sisson et al., 2014]. Basaltic lavas were also documented up to 30 km to the north at the Three Sisters and Dalles Lakes vents [*Reiners et al*., 2000]. Compared to the bulk of volcanic products documented elsewhere along the Cascades magmatic arc, those erupted by Mount Rainier stand out because their geochemistry indicates a slab signature [*Leeman et al*., 2005]. A direct link to the slab is also supported by geophysical studies. Using a combination of magneto-telluric and seismic data, *McGary et al*. [2014] imaged a conductive body emanating from the top of the slab that has properties consistent with a melt fraction of 2% and 10 wt % water in the melt. Mount Rainier is surrounded by Eocene continent-derived sedimentary rocks to the west and southeast, which have been proposed to underlie the volcanic edifice [*Sisson et al*., 2014]. The crust is locally intruded by granodioritic plutons such as the 19–14 Ma Tatoosh intrusive suite [*du Bray et al*., 2011]. Mount Rainier coincides geographically with the boundary of a large north-south trending electric anomaly known as the Southern Washington Crustal Conductor (SWCC hereafter) [*Egbert and Booker*, 1993]. The SWCC could represent marine sediment trapped during tectonic accretion [*Stanley et al*., 1992] or a large zone of partial melting in the middle crust also feeding Mount St. Helens and Mount Adams [*Hill et al*., 2009].

3. Data

The majority of the stations used here are broadband instruments from the CAFE experiment [*Abers et al*., 2009], deployed from 2006 to 2008. We also use several stations from the Earthscope Transportable Array and permanent broadband stations from the Cascade Volcano Monitoring network and from the Pacific Northwest Regional Seismic Network (Figure 1). The stations used to obtain ambient noise cross correlograms and phase velocities represents a subset of that previously analyzed by *Calkins et al*. [2011], and all lie within 150 km of Mount Rainier. This subset is intended to be small enough to capture small-scale variations, but broad enough to provide good resolution at the limited number of sites used for joint RF-dispersion analysis. The joint inversion of receiver functions and phase velocities were performed using the 15 closest stations to Mount Rainier (Figure 1).

4. Methods

4.1. Receiver Functions

To calculate receiver functions, we select events with magnitude larger than 5.5 and epicentral distance between 30° and 90°. Raw data are first filtered using a zero-phase third-order Butterworth filter with a passband of 0.01–0.5 Hz, and we discard all events with signal-to-noise ratio smaller than 5 on the radial components. We generate RFs with the time domain deconvolution method developed by *Ligorría and Ammon* [1999], and accept those for which the radial RF, when convolved with the observed vertical component, matches the observed radial component seismogram above a predefined threshold of 75% RMS signal amplitude. The Gaussian filter used during the deconvolution process has a characteristic frequency f_c of 0.45 Hz:

$$H(f) = \exp\left(-0.5\left(\frac{f}{f_c}\right)^2\right).$$

Complex structures involving scatterers, dipping interfaces, and/or anisotropy cause RF waveforms to vary as a function of back azimuth. Since we use temporary stations with limited azimuthal coverage of sources, we cannot fully resolve the azimuthal variations in RF waveforms as required to model anisotropy or dipping interfaces. We thus choose to assume a locally flat layered and isotropic structure, but treat different back-azimuthal ranges separately. Most events that provided well-constrained RFs come either from the WNW (back-azimuth of 270–330°) or from the ESE (90–150°) and are thus gathered and stacked accordingly, after visually checking they are consistent (see event map in supporting information). The number of individual RFs in each stack averages 30 and ranges from 9 to 99. For the purpose of joint RF-surface wave dispersion inversion, the ESE and WNW RF stacks for each station were used independently in two separate inversions. Differences between the resulting velocity models from the two back-azimuthal bins give a diagnostic of how the final velocity model is affected by anisotropy or dipping interfaces (see section 5). The inversion uses the *P* wave coda up to 30 s after the direct *P* wave arrival. Although the fit of the last 20 s is

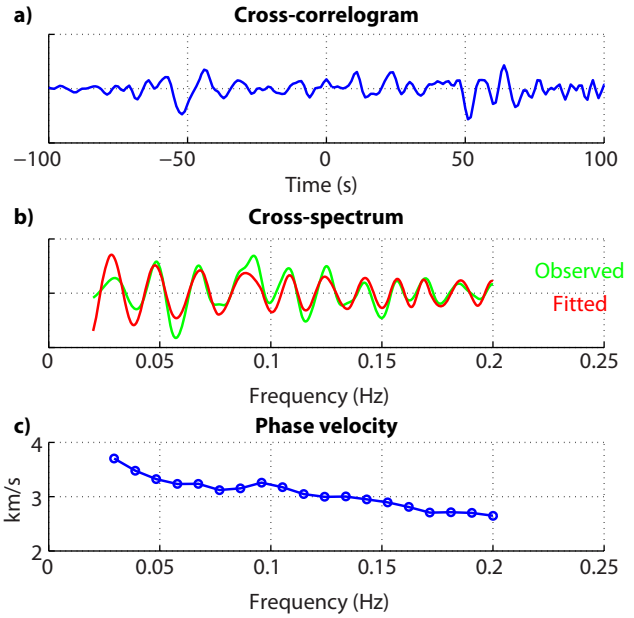

Figure 2. Example of a phase velocity measurement obtained using the approach proposed by *Ekström et al*. [2009]. The distance between the stations (BD11-E03A) is 147 km. (a–c) The average cross correlogram, the real part of the associated cross-spectrum, and the estimated phase velocity using Aki's formulation, respectively (see section 4).

often poorer than for the first 10 s, using a long coda stabilizes the inversion by preventing models producing large-amplitude coda from being accepted.

4.2. Surface Wave Dispersion Measurements

We calculate short period dispersion constraints in the range 7–21 s using ambient noise [*Shapiro and Campillo*, 2004], updating the results of *Calkins et al*. [2011] for the study region. To obtain cross correlograms we first process the seismic noise records following the standard approach described in *Bensen et al*. [2007]. Noise records are cut into daylong time series, filtered between 0.003 and 0.3 Hz, and whitened used the 1 bit method. The number of days of recording averages 313 and ranges from 60 to 625. Preprocessed noise samples are cross correlated in the frequency domain for each pair of stations. Subsequently, rather than using the traditional frequency-time analysis, or FTAN [*Dziewonski et al*., 1969], to estimate the phase velocity, we apply the frequency domain method proposed by *Ekström et al*. [2009] based on Aki's formulation [*Aki*, 1957]. The azimuthally averaged normalized cross spectrum $\bar{\rho}(r,\omega_0)$ for the interstation distance r and frequency ω_0 varies as a zero-order Bessel function of the first kind J_0, which can be fitted to estimate the phase velocities $c(\omega_0)$ (Figure 2):

$$\bar{\rho}(r,\omega_0)=J_0\left(\frac{\omega_0}{c(\omega_0)}r\right).$$

The main advantage of this approach is that the interstation distance required to make measurements can be reduced to 1 wavelength or less, as demonstrated empirically by *Calkins et al*. [2011], thus allowing longer periods for a given pair of stations. All individual dispersion curves (station pairs) are combined and inverted tomographically to obtain phase velocity maps on a 0.125° × 0.125° grid. We apply damping and choose the value that maximizes the variance reduction while keeping the model as smooth as possible. We then extract phase velocities at the sites corresponding to each station targeted for joint inversion. These dispersion constraints at periods of 7–21 s are combined with longer-period ones (25–100 s) resolved from teleseismic surface waves by *Foster et al*. [2014]. The authors obtained two-station phase measurements by differencing single-station phase measurements made on earthquake data recorded on the USArray Transportable Array. A correction to the two-station geometry was made for off-great-circle arrivals. The two-station phase measurements with interstation path lengths between 350 and 750 km were inverted on a 0.5° × 0.5° grid to produce Rayleigh wave phase-velocity maps.

4.3. Joint Inversion Scheme

To jointly invert the RFs and dispersion constraints, we make use of a Bayesian trans-dimensional inversion scheme [*Bodin et al*., 2012]. As in most joint inversion schemes developed for the specific purpose of jointly inverting RF and dispersion curves [*Julia et al*., 2000; *Shen et al*., 2013a], the model space parameters include the thickness of each layer and corresponding shear velocity. In this study, we impose $V_P/V_S = 1.8$ in all layers. We test other values for V_P/V_S between 1.7 and 1.9. The choice of V_P/V_S within this range does not affect the first-order structure, and we find that 1.8 produces the best fit. We also modified the joint

inversion scheme to let V_P/V_S be a parameter to resolve, but we found that the resulting values were poorly constrained and thus only report results for preassigned V_P/V_S. The a priori number of layers is poorly known [*Malinverno*, 2002], so it is treated as a parameter to be resolved. Any layer that does not improve significantly the fit to the data, given the level of noise, will be removed during the model exploration, minimizing the number of layers. Finally, because processing and stacking make the level of noise difficult to estimate, especially for the RF, noise is also treated as a parameter of the model space. Following *Bodin et al*. [2012], here, we assume uncorrelated and correlated Gaussian noise for the dispersion curves and RF, respectively. The RF noise covariance matrix is defined based on the width of the Gaussian filter used during the deconvolution.

At each step of the inversion, a move is randomly selected among five possibilities: (1) modifying the velocity of a randomly selected layer, (2) modifying the thickness of a randomly selected layer, (3) creating a new layer at a random depth, (4) deleting an existing layer randomly selected, and (5) randomly modifying the estimated noise level. The alterations to the parameters all follow a Gaussian law with predefined half width chosen so that the acceptance rate of each individual type of move is close to 44%, which is the optimal value for an efficient model sampling [*Rosenthal*, 2000]. Models falling outside predefined bounds are immediately rejected. For each move, the likelihood is calculated and compared to that of the latest accepted model to estimate its acceptance probability. The move is accepted if that probability is larger than a randomly generated number between 0 and 1. We run 500,000 iterations for each inversion. The final model is defined as the median over the last 80% of the accepted models (the first 20% of them represent the "burning-in phase"). To make sure that the final model does not depend on the starting one, for each station we run several inversions using distinct starting models.

The level of noise controls the relative importance of each data set, so there is no need to define weights. Since the estimated noise governs how much the inversion scheme tries to fit the data, the larger it is, the smaller number of layers will be used to improve the fit. Of course, any real feature in the observed data (as opposed to random noise) resulting from structural complexity not accounted for in our forward modeling, such as anisotropy, will be considered as noise by the algorithm and will thus increase the estimated level of noise. The approach does not impose any regularization (damping, smoothing between adjacent layers), as the surface wave constraints have a significant effect on the stability and smoothness of the model.

5. Results

5.1. Phase Velocity Maps

Figure 3 shows the ray path coverage and checkerboard resolution tests for the noise-based velocity maps at periods of 7, 13, and 21 s. The input velocity is 3 km/s $\pm$ 5%. This test shows that large (0.5° $\times$ 0.5°) and even small (0.25° $\times$ 0.25°) anomalies should be well recovered at all stations used for the joint inversion. Actual phase velocity maps are shown in Figure 4 for the same periods, which have maximum sensitivity around 9, 18, and 27 km depth, respectively. At 7 s, the main feature is a faster region that correlates with the boundaries of the Ancestral Cascades. These fast anomalies contrast with slower regions below the forearc to the west and with the High Cascades to the southeast. This pattern persists at 13.0 s period, but the correlation with the surface geology is less clear. At 13 s period, comparatively slow velocities of around 3.1 km/s are observed just east of Mount Rainier, near Mount Adams and Goat Rocks. At 21 s, this slow feature persists, with a prominent low-velocity anomaly (V_S = 3.1 km/s) east of Mount Rainier.

Although the phase velocity maps shown in Figure 4 are not directly comparable to three-dimensional velocity models, we can compare them with the regional shear velocity tomograms obtained by *Gao et al*. [2011] and the local *P* wave model obtained by *Moran et al*. [1999]. Gao et al.'s model exploits ambient noise as in our own study, but uses only TA stations around Mount Rainier spaced at 70 km, which should result in lower spatial resolution (no checkerboard resolution test is provided). *Gao et al*.'s model captured the same velocity contrasts between fast velocities underlying the Ancestral Cascades and slow velocities to the east and west in the upper and middle crusts. However, at lower-crustal depth, their model shows slow velocities right beneath Mount Rainier, while our study shows a similar slow region slightly offset to the east-southeast. The sensitivity kernels of Rayleigh waves at periods of 7, 13, and 21 s peak at roughly 9, 18, and 27 km depth, respectively, and can be compared to layers 4, 6, and 7 from *Moran et al*. [1999]. These authors also observed faster velocities below the Ancestral Cascades with a slower region east and

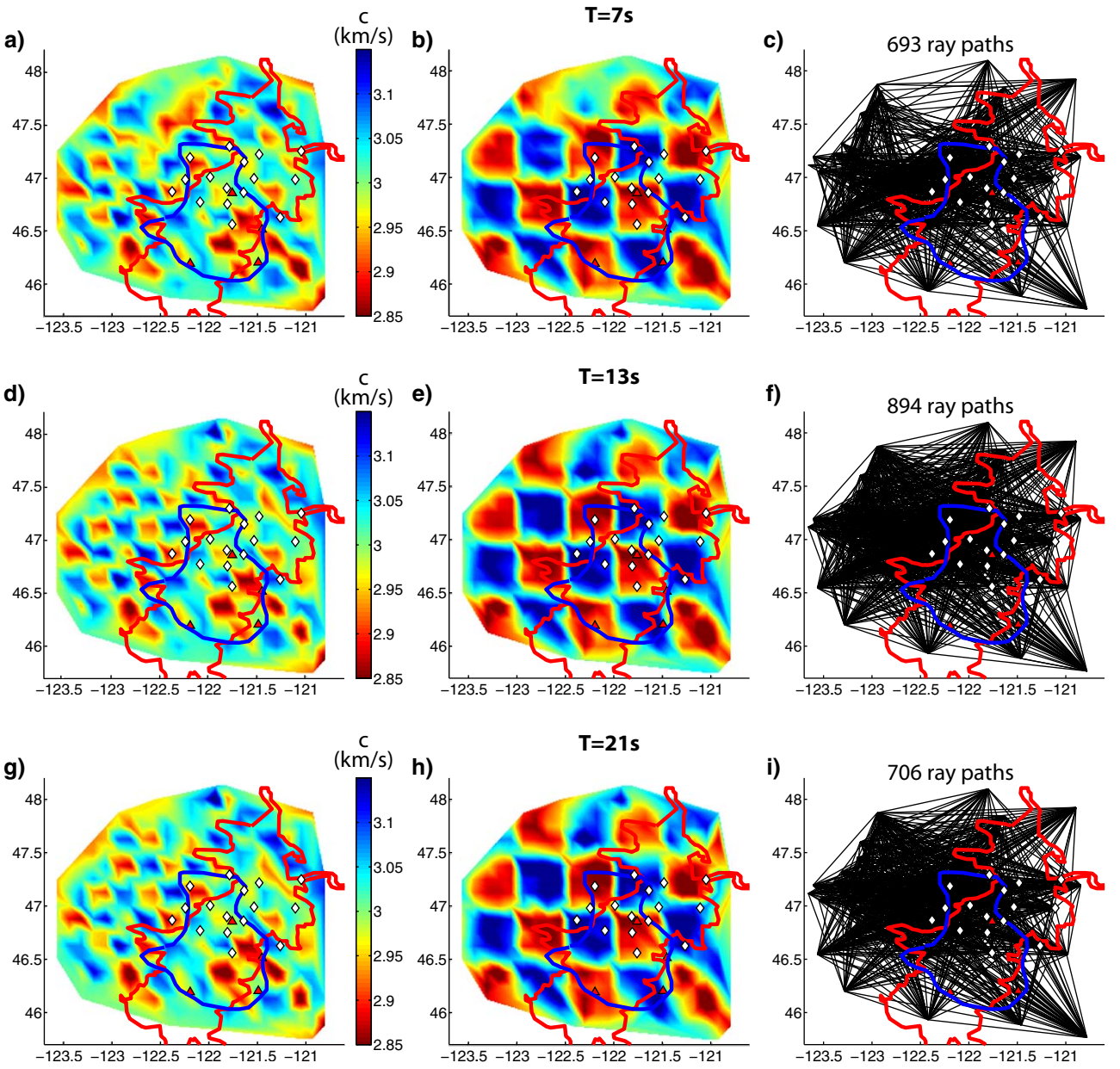

Figure 3. Checkerboard resolution tests and ray path distributions for periods of 7, 13, and 21 s. The input phase velocity for the checkerboard test is 3 km/s ± 5%, for anomalies sized (a, d, g) 0.25° × 0.25° and (b, e, h) 0.5° × 0.5°. (c, f, i) The right column shows the corresponding ray path coverage. Lines and symbols same as Figure 1.

southeast of Mount Rainier. Nevertheless, while we observe slower shear velocities west of the Ancestral Cascades at all depths, their P model is slow in that region in the upper crust only. Moran's model and ours are well resolved in that region, although the crustal body wave data has relatively less resolution below 18 km. It is possible that this discrepancy between shear and compressional models is real, such as would result from the presence of fluid released by the subducting slab, which affects shear velocity more significantly than compressional velocity. However the local P tomography relies upon diving rays below 10–15 km depth and ray coverage is highly nonuniform, so it is difficult to be sure the difference is not caused by resolution issues with the P tomography.

5.2. Joint Inversions

Figure 5 shows the velocity models obtained for station N100 by jointly inverting the RFs and phase dispersion constraints, along with the corresponding data fits. This station lies 50 km north of Mount Rainier

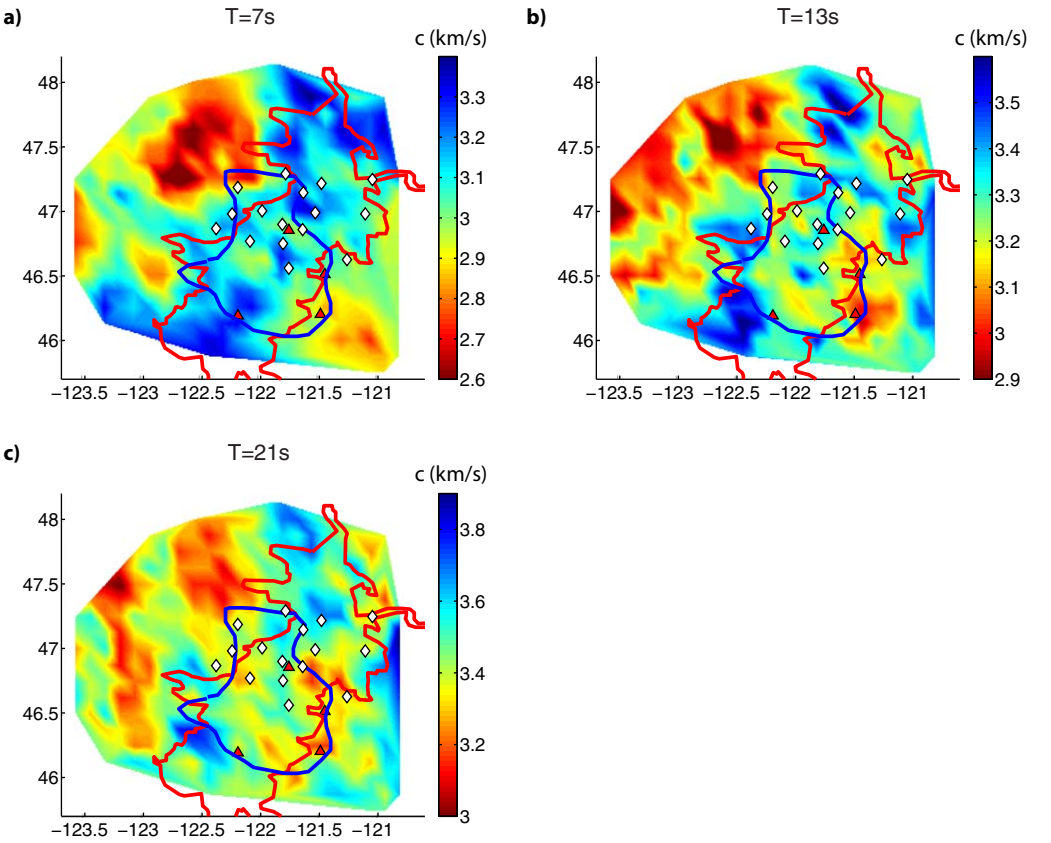

Figure 4. Phase velocity maps from ambient noise tomography at periods of 7, 13, and 21 s. Rayleigh wave sensitivity for each period peaks around 9, 18, and 27 km depth, respectively. Lines and symbols same as Figure 1.

(Figure 1). The RFs exhibit azimuthal variations in the timing and amplitude of the phases making up the waveforms. The same observation holds for most stations used in this study (Figure 6 and supporting information Figure A1), and confirms that, as expected, the structure below Mount Rainier and surrounding regions is more complex than a stack of flat and isotropic layers. In spite of the simple isotropic/flat layered modeling assumed here for RF forward calculations, we note that for N100 and most other stations, the velocity models resulting from using the two different RF azimuthal stacks are very similar (Figures 5 and 6). Several stations, notably PANH, and S080, do exhibit V_S discrepancies between back-azimuths at some depths.

Overall, the models fall into two main groups (Figure 6). Group I includes stations located east of Mount Rainier, at the transition between the Ancestral and the High Cascades (E060, N130, S100), plus station N110. These velocity models exhibit velocities of $3.4 \leq V_S \leq 3.8$ km/s at 25 km depth, a sharp Moho, and $4.2 \leq V_S \leq 4.4$ km/s at 50 km depth. Group II includes sites located in the Ancestral Cascades (E05A, E050, LON, N100, N120, OBSR, PANH, S080, S090) and west of it (S065, S070). In this group, the lower crust and uppermost mantle are on average faster (by 0.2 km/s at 25 km depth, $3.5 \leq V_S \leq 4.1$ km/s) and slower (by 0.2 km/s at 50 km depth, $3.9 \leq V_S \leq 4.3$ km/s) than for Group I, respectively. This yields a weak to absent Moho. The E-W contrast in uppermost mantle velocities east of Mount Rainier also clearly appears in the noise-based model constrained by *Gao and Shen* [2014]. Note that the distinction between Groups I and II is not always unambiguous. For example, E060 displays lowermost crust and uppermost mantle that are not as low as N110 and as fast as N130, respectively. Nevertheless, the velocity structure of E060 is still closer to that of these two stations than to that of typical Group II station like LON. Station OBSR, the closest to the Rainier summit, exhibits significant fluctuations in the uppermost mantle. While this feature consistently appears in both RF azimuthal bins, we consider this feature as physically unlikely and perhaps an artifact of assuming one-dimensional structure in the highly heterogeneous volcanic conduit environment.

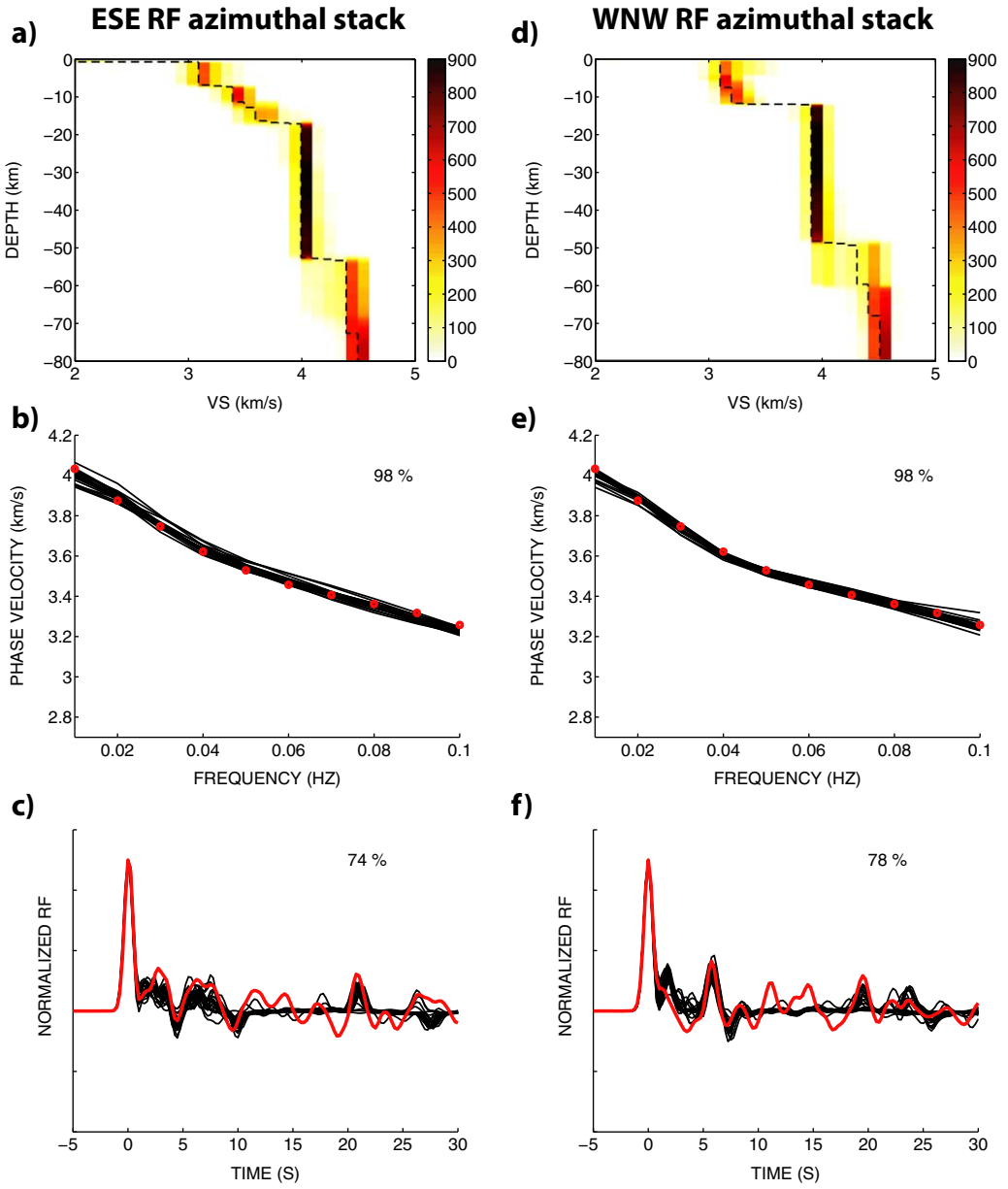

Figure 5. Shear velocity models from joint inversion and fit for station N100. Left and right columns are for the ESE (90–150°) and WNW (270–330°) RF azimuthal stacks. The top plots show the color-coded hit counts of the model space, a representation of the probability density function. Only 1 out of 10 of the accepted models are shown, minus the first 20% ("burning-in phase"). The black dashed lines are the median at each depth. The center and bottom plots show (b, e) dispersion curves and (c, f) RFs corresponding to a selection of accepted models. The RFs amplitude is normalized. The red lines are the data and the number on the plot is the variance reduction.

Figures 7 and 8 show map views and vertical cross sections through the velocity profiles. Both figures emphasize the roughly E-W contrasts between the structure observed along the center of the arc and the surrounding regions, with faster crust and slower mantle below the active volcanic region. When observable, the inferred depth of the Moho (defined as the depth at which $V_S = 4$ km/s) ranges between 35 and 45 km. This range compares well with results from *Shen et al.* [2013b], obtained by applying a joint inversion scheme that combines RFs and surface wave dispersion measured at stations from the USArray. In particular, *Shen et al.* [2013b] observed the eastward increase in the Moho sharpness. The Moho clearly appears as a sharp contrast in Figure 8 below S100 and N110, but is weak or absent along the rest of the cross sections. Overall, the depth we infer is in good agreement with the model of *McGary et al.* [2014], which shows a flat Moho at ~40 km depth below and east of Mount Rainier.

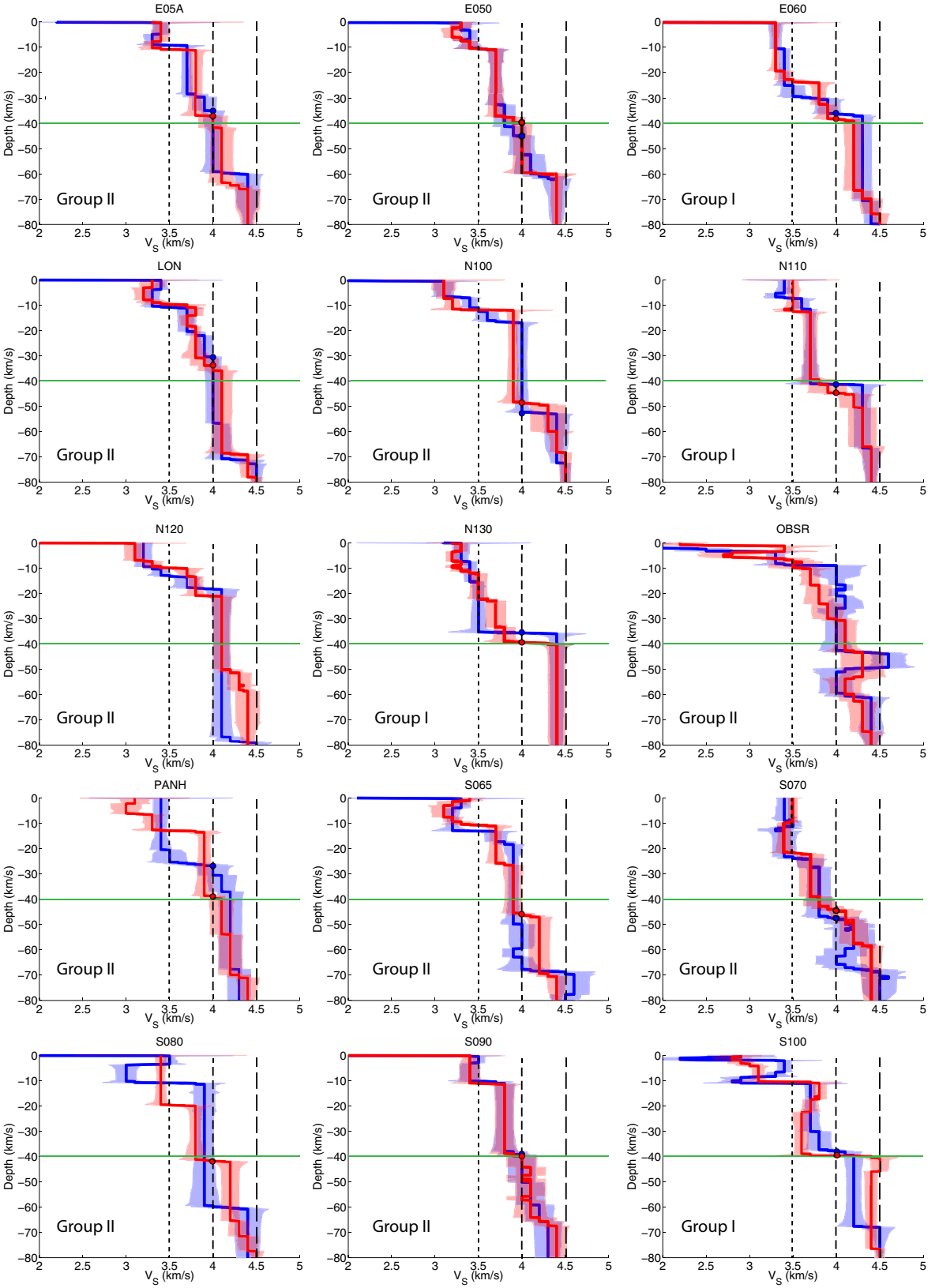

Figure 6. Shear velocity models from joint inversion at all stations. The lines show the median of all accepted models using the WNW (red) and ESE (blue) RF azimuthal stacks. The shaded area indicates 1 standard deviation. The vertical lines are plotted at 3.5, 4, and 4.5 km/s and the horizontal lines at 40 km are plotted to make comparisons between models easier. The group of each station is indicated at the bottom left of each plot. The dot indicates our pick for the crust-mantle transition.

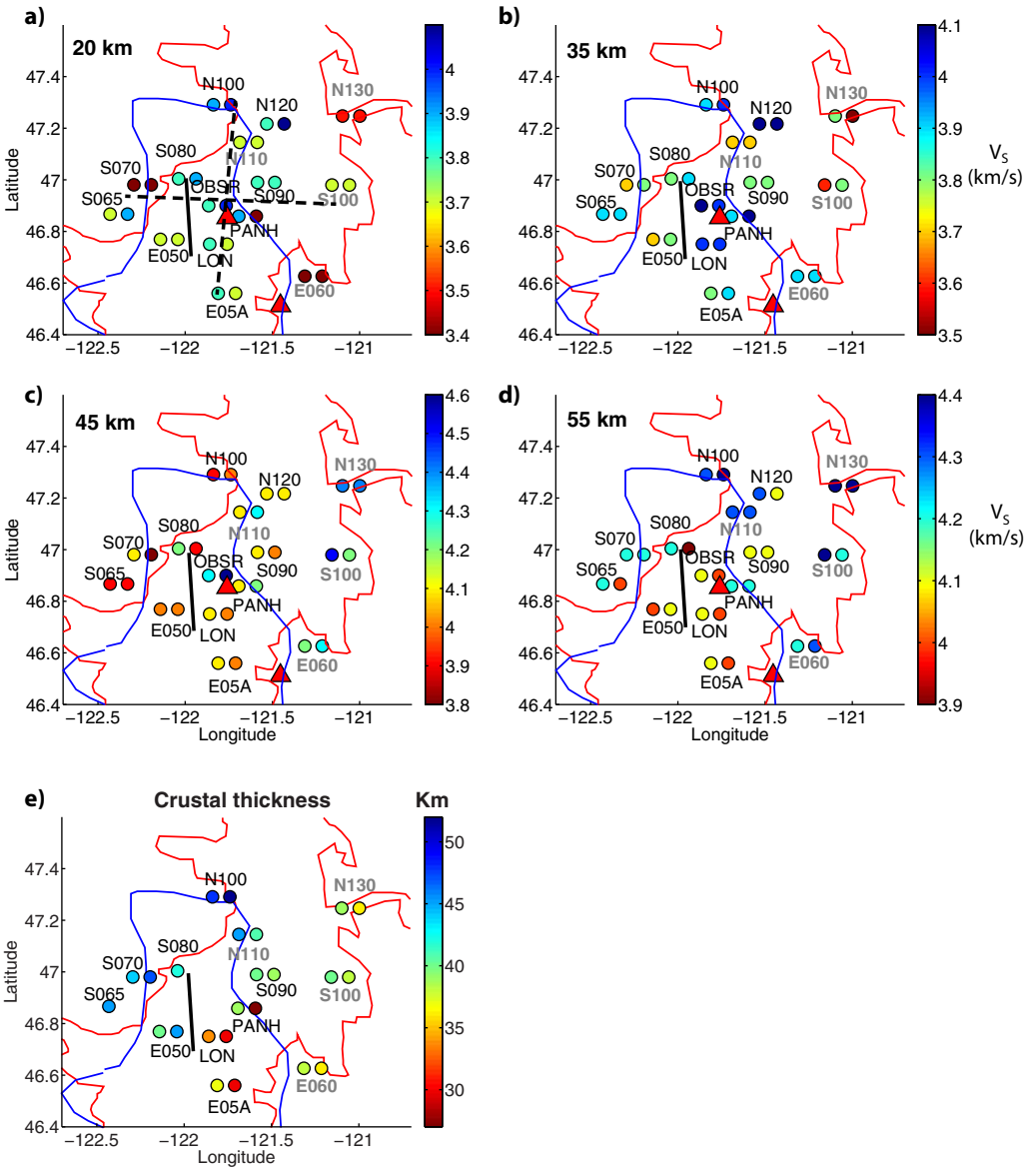

Figure 7. Map view of the final V_S models at all stations. (a–d) V_S distribution at 25, 35, 45, and 55 km depth. For each station, two color-coded dots indicate V_S constrained from the two RF azimuthal stacks (ESE versus WNW). The dashed lines in Figure 7a indicate the location of the roughly EW and NS transects displayed in Figure 8. Stations belonging to Group I are labeled in gray. Lines and symbols same as Figure 1. Panel (e) maps the depth of the Moho as defined as V_S = 4 km as picked in Figure 6.

6. Discussion

6.1. Crustal Composition

To understand the nature of the crust, we compare the velocities of Groups I and II with theoretical velocities obtained from a range of possible rock assemblages. We use representative lithologies from the compilation of rocks collected around Mount Rainier [*Sisson et al.*, 2014], for a wide range of silica contents that illustrate the range of possible basement compositions. These samples come from the Eocene-Paleocene Siletz basalts (sample 08KS1011, 47.4 wt % SiO_2), a gabbronorite inclusion from the Mount Rainier eruptives (sample 93RE16, 56.08 wt % SiO_2), the Miocene Tatoosh granodiorite (sample 93T59, 66.8 wt % SiO_2), and two common sedimentary units, the Mesozoic Russell Ranch arkose (sample 09RR1001, 71.9 wt % SiO_2) and the Paleogene Puget Group arkose (sample 08W1012, 84.5 wt % SiO_2). For the igneous rocks, we estimate the modal mineralogy from major element chemistry using the Perple_X free-energy minimization algorithm [*Connolly*, 2005] with solution models and other parameters as described by *Jagoutz and Behn* [2013].

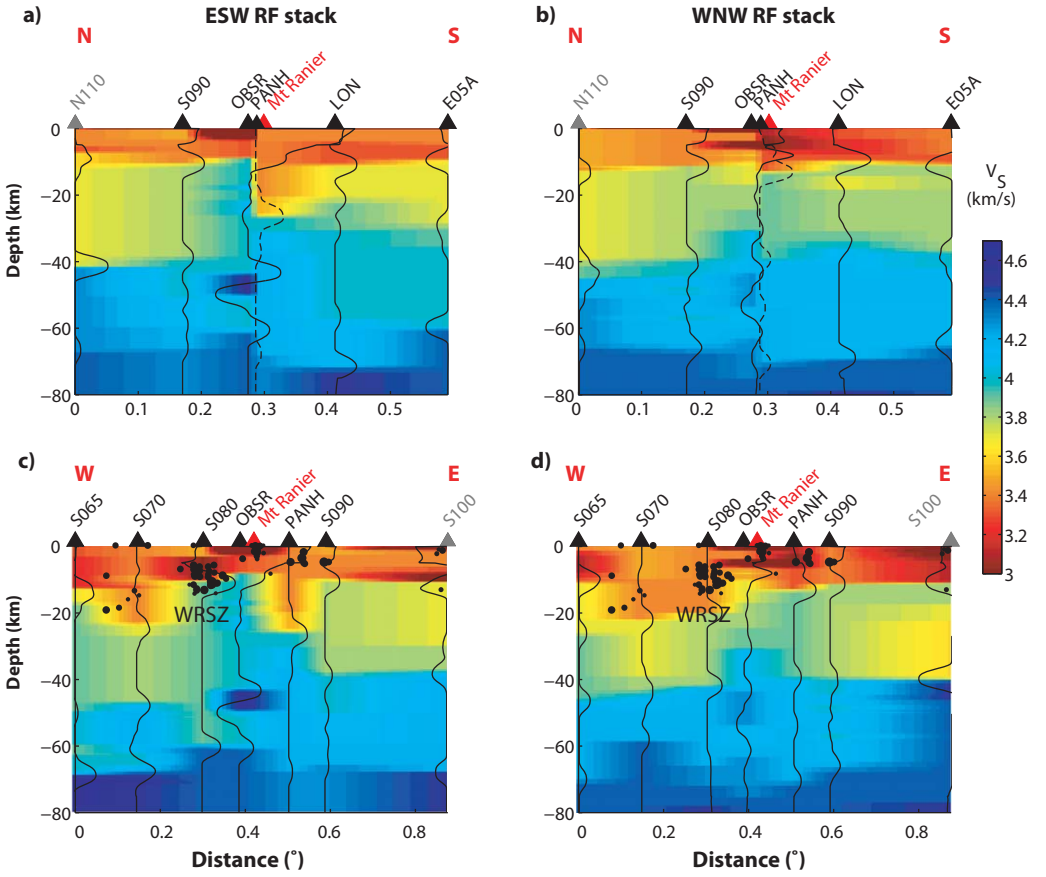

Figure 8. Vertical slices through the final V_S models obtained using (a, c) the ESE RF azimuthal stack and (b, d) the WNW stack. These 2-D velocity profiles were obtained by fitting a surface between the 1-D velocity models at stations along the roughly EW and NS transects displayed in Figure 7a. The vertical line below each station shows the derivative of the smoothed velocity profiles and gives a measure of the sharpness of each contrast. Stations belonging to Group I are shown in gray. Seismicity with M > 1 recorded since 1970 between 46.74°N and 47.14°N is shown in Figures 8c and 8d and highlights the West Rainier Shear Zone (WRSZ).

Because reactions are unlikely to proceed to equilibrium at low-temperature conditions, mineralogy is calculated with a minimum temperature fixed at 700°C for anhydrous compositions (basalt and gabbronorite) or 500°C for the granodiorite; to produce the observed hornblende, 0.4 wt % H_2O was assumed present in the Tatoosh granodiorite. For sedimentary rocks, not necessarily in chemical equilibrium, we approximated dominant mineralogy from published descriptions of these and analogous rocks. We then calculate shear velocity with the approach developed by *Hacker and Abers* [2004], at predicted temperature and pressure. We estimate two geotherms by combining the values for the conductivity (2.5 and 3.1 W/m/K for the crust and mantle, respectively) and radiogenic heat (1.3, 0.4, and 0.02 μW/m^3 for $0 < z < 10$ km, $10 < z < 40$ km and $z > 40$ km, respectively) taken from *Currie et al.* [2004], and a surface heat flow of 60 or 80 mW/m^2 [*Blackwell et al.*, 1990]. These two geotherms predict temperatures at 40 km depth, the nominal Moho, of 690°C and 850°C, respectively (see supporting information).

Figure 9 shows the observed V_S compared to those predicted for these five sample suites with different assumptions about chemical equilibrium, along with single-mineral velocities of several common minerals. This comparison shows that even though there is a good agreement between the average velocity of Groups I and II and some rock compositions, none of them can explain the low midcrustal velocities of Group I. Part of the problem is that V_S for quartz, unlike V_P, is considerably higher than that of plagioclase so that V_S does not decrease with increasing silica content. Some phenomenon other than composition likely reduces the shear velocity here. A range of compositions can fit the Group II middle crust, depending upon equilibrium assumptions. The Siletz basalt and Tatoosh granodiorite equilibrium models significantly overpredict V_S at >20 km depth, where garnet is stable and increases predicted velocities, an effect seen in larger compilations [*Behn and Kelemen*, 2006]. Increasing the geotherm to raise Moho temperatures by 300°

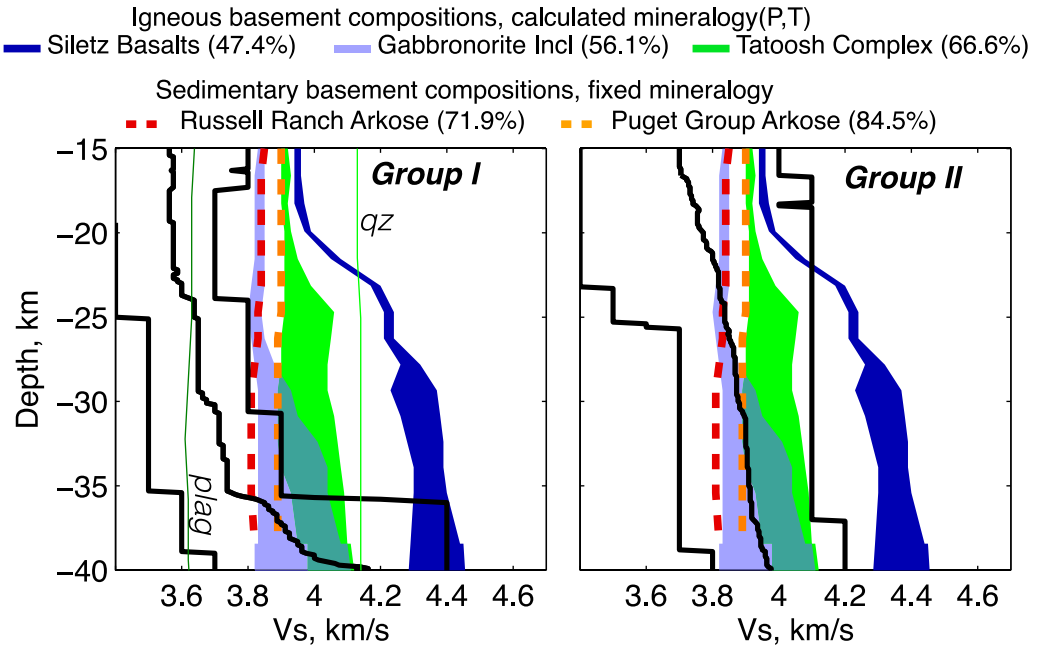

Figure 9. Comparison between observed crustal *S* wave velocities and those predicted for the composition of rock samples from basement rocks collected around Mount Rainier and described in *Sisson et al.* [2014]. For each group, black lines show the average, minimum, and maximum V_S obtained from the joint inversion at each depth. Predicted model velocities are calculated for representative compositions along the geotherm as described in the text, spanning a wide range of silica contents (47.4–84.5 wt % SiO_2). Shaded areas show results for the labeled igneous compositions (wt % SiO_2 in parentheses), calculated at equilibrium conditions via Perple_X [*Connolly*, 2005], bounded by geotherms producing 60 and 80 mW/m^2 for approximate Moho temperatures of 700°C and 850°C. Silicic sedimentary mineralogies are determined from petrologic descriptions and assumed to be unchanged with pressure; predicted velocities for these compositions are shown with dashed lines. Thin lines show predicted V_S for common crustal minerals: qz, quartz; plag, plagioclase (an50); opx, orthopyroxene (equal parts Mg and Fe end-members); and cpx, clinopyroxene (80% diopside, 20% hedenbergite).

only reduces these velocities by 0.1–0.15 km/s for the basalts, but more so for the granodiorites because major phase boundaries are crossed.

We also compare our average velocity profiles to the set of theoretical shear velocities obtained by *Jagoutz and Behn* [2013] based on exposed arc sequences worldwide. Figures 10a and 10b display the shear velocity from their compilation as a function of SiO_2 and FeO + MgO contents, at a nominal lower-crustal temperature (550°C) and pressure (0.8 GPa), corresponding to the geotherm used here and just outside the primary garnet stability field. These plots show that, although V_S correlates with the major oxide content, V_S shows much scatter for any given SiO_2 content. As discussed above, average V_S does not vary with silica for >60% SiO_2, in marked contrast with the strong correlation with V_P more commonly used to infer silica content [*Behn and Kelemen*, 2006; *Rudnick and Fountain*, 1995]. V_S does vary with FeO + MgO for these high-silica compositions (Figure 10b), so may provide other useful information regarding crustal composition. Figures 10c–10f show the theoretical and observed velocities as a function of depth using the geotherm described earlier. The theoretical velocities are split into 10% wide bins in SiO_2 or (FeO + MgO) from the *Jagoutz and Behn* compilation. For example, the dark blue line in Figure 10c is the average V_S for all rocks with $40 \leq SiO_2 \leq 50\%$. The corresponding shaded area shows one standard deviation. This comparison shows that the range of lower crust velocities spanned by Group II can be explained by rock assemblage containing between 50% and 80% SiO_2 (diorite to granite) and less than 20% FeO + MgO. We note that the α- to β-quartz transition has little effect on shear modulus [*Ohno et al.*, 2006], so these V_S measurements are relatively insensitive to it.

Both of these comparisons (Figures 9 and 10) seem to exclude the conspicuous presence of mafic or ultramafic rocks in the lower crust, such as might be described by the Siletz Basalt composition at these depths (Figure 9). This contrasts with oceanic arcs globally, which typically show fast lower crust compared with continent [*Calvert et al.*, 2008] and are consistent with low silica compositions [e.g., *Tatsumi et al.*, 2008]. The main obvious distinction is that the arc here is built on preexisting crust, unlike oceanic arcs. Hence, the

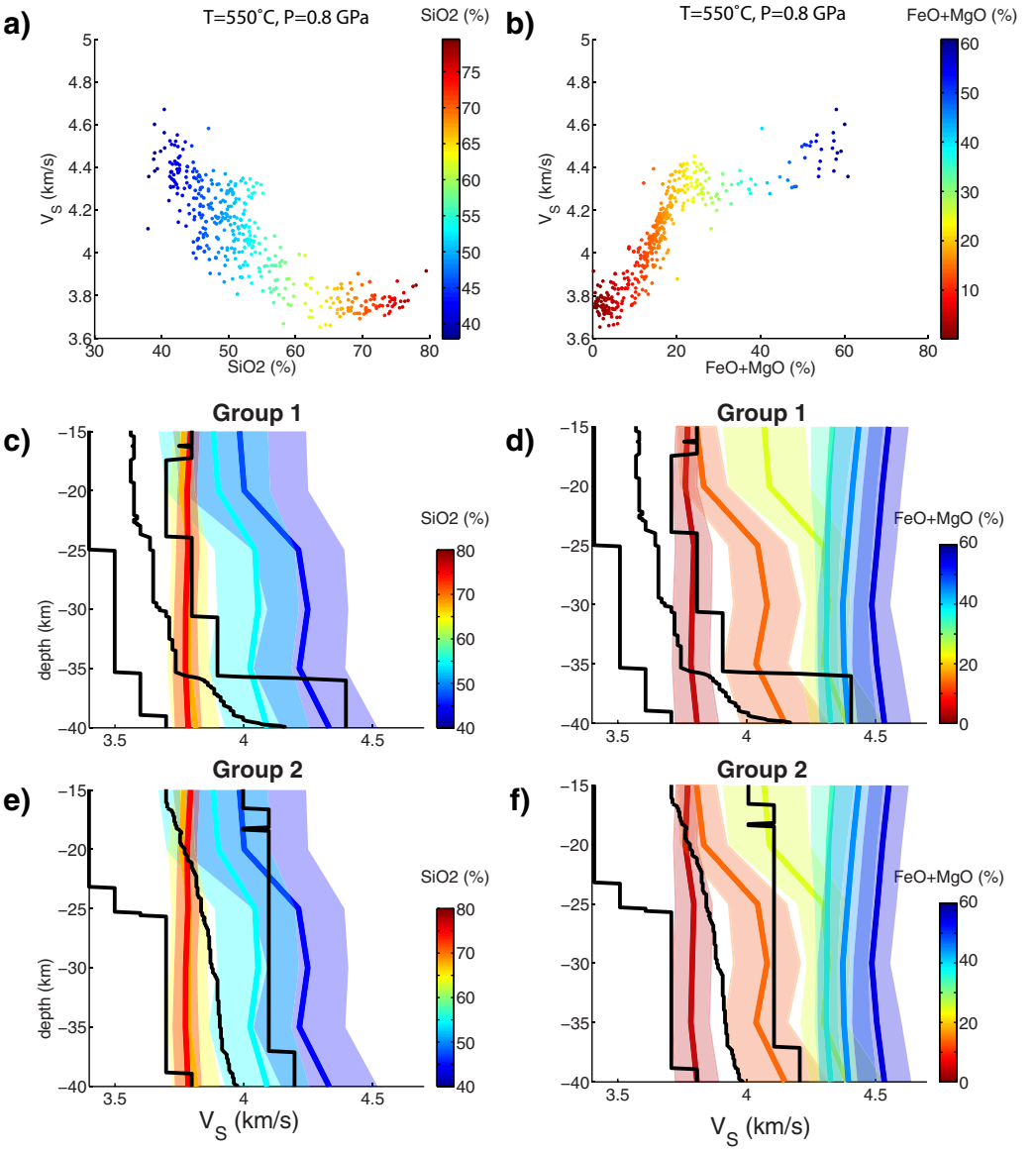

Figure 10. Comparison between observed crustal velocities and the theoretical shear velocities obtained by *Jagoutz and Behn* [2013] based on exposed magmatic arc rocks globally. Figures 10a and 10b display the shear velocity as a function of SiO_2 and FeO + MgO contents. Figures 10c–10f compare the theoretical and observed velocities for Groups I and II. The theoretical velocities are split into 10% wide bins in SiO_2 or (FeO + MgO) and averaged. The solid lines and shaded areas indicate the mean and standard deviation in each bin. For each group, the left, middle, and right black lines are the minimum, average, and maximum observed value at each depth.

velocities of Group II and inferred composition do not seem to indicate the presence of the mafic rocks of the Siletzia Terrane, which should exhibit faster V_S. We note that many Group II stations lie well west of the magmatic front so should be unaffected by melts (Figure 1). Our results thus suggest that the edge of the Terrane is buried further west. The highest lower-crustal velocities ($V_S \geq 4.1$ km/s) at station OBSR and PANH located close to Mount Rainier are indicative of intermediate composition or even something as felsic as the Tatoosh granodiorites, which is consistent with the dominantly andesitic volcanic products found in this area. These seismic anomalies near the volcanic centers could be explained by a lower crust composed of a mushy andesitic crustal magmatic system and solidified intrusion along the volcanic conduits as suggested by *Sisson et al*. [2014]. High lower-crustal velocities ($V_S = 4.1$ km/s) at station N120 are more enigmatic, as this station is located away from Rainier. We can speculate that the inferred intermediate composition is associated with the plumbing of the Dalles Lakes vents or past magmatism. The felsic-to-intermediate composition inferred for the other stations forming Group II may represent magmatically more evolved crust.

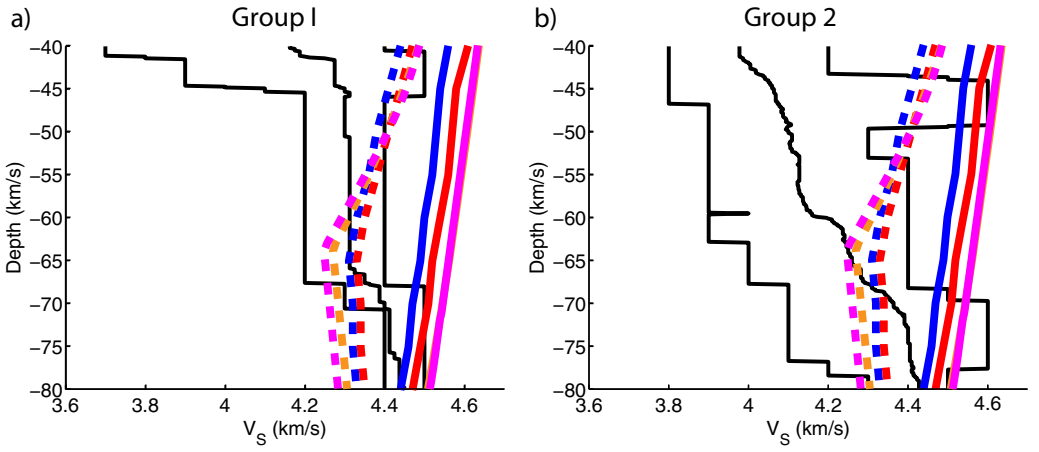

Figure 11. Comparison between observed upper mantle velocities (black lines, left to right: minimum, average, and maximum values) and theoretical values for harzburgite (red), lherzolite (blue) and olivine as calculated using the framework from *McCarthy and Takei* [2011] (pink) and *Jackson and Faul* [2010] (orange). The solid pink and orange lines fully overlap. Calculations were performed using two geotherms, one based on the surface heat flow (60 mW/m^2, solid lines) measured at Mount Rainier [*Blackwell et al*., 1990] and a higher value (80 mW/m^2, dashed lines).

However, the analysis of geochemical and isotopic composition of Mount Rainier andesites suggests modest chemical differentiation in the crust [*Sisson et al*., 2014]. Therefore, this part of Group II most likely represents the prearc basement.

We see lower velocities in the midcrust west of the West Rainier Shear Zone (WRSZ), 15–20 km west of the Rainier summit, than farther east. The inferred westward transition from intermediate rocks (OBSR) to more felsic rocks (S080) coincides with the location of the WRSZ (Figures 7, 8c, and 8d). This observation supports the role played by the movement of magma and/or hydrothermal fluids in the middle-lower crust in the triggering of local seismicity, as proposed by *Nichols et al*. [2011]. By contrast, *Moran et al*. [1999] observe lower velocities east of the WRSZ, although they only have upgoing rays in the upper 10–15 km so it is difficult to be sure deeper structures are resolved. Their observation may reflect low upper-crustal velocities within 10–15 km of the volcanic edifice associated with the shallow magmatic system, which we cannot resolve.

Finally, based on our rock compilation, we cannot explain the very low velocity observed below stations of Group I (V_S = 3.4 km/s at 25 km depth) based on temperature or composition. Stations located to the east of the Ancestral Cascades, i.e., E060, N130, and S100, all coincide with subduction melanges ranging from nonmetamorphosed to blueschist facies, a close analog to the Franciscan Formation in California. The fractured nature of these rocks may produce high porosity that would explain the lower V_S, since poroelastic effects on shear modulus are strong [*Takei*, 2002], although this would require pores to remain open deeper than typically assumed [*Yardley and Valley*, 1997]. Except for station N110 these stations lie >20 km east of the magmatic front, so the presence of partial melt seems like a less likely explanation.

6.2. Physical State of the Uppermost Mantle

To assess the state of the uppermost mantle, we calculated shear velocity for two mantle peridotites, a harzburgite and a lherzolite with compositions described by *Hacker et al*. [2003], using the geotherm described above (690°C and 850°C at 40 and 55 km, respectively) and the approach of *Hacker and Abers* [2004]. To evaluate the possible effect of attenuation on mantle velocities, we also compare our observed velocities with pure olivine velocities corrected for physical dispersion as calibrated in laboratory experiments [*Jackson and Faul*, 2010; *McCarthy and Takei*, 2011]. As shown in Figure 11, all the theoretical velocities are larger than observed (with the exception of OBSR which exhibits suspicious fluctuation in the uppermost mantle). By using a hotter geotherm based on a heat flux of 80 mW/m^2 (1100°C and 1270°C at 40 and 55 km, respectively) we can match the velocity of Group I. Nevertheless, upper mantle average velocity for Group II is still much slower than the theoretical values (4.1 km/s at 55 km depth). Assuming the hotter geotherm, the velocity should be ∼4.4 km/s for both harzburgite and lherzolite (Figure 11), ∼7% higher than observed.

One possible explanation for the slow anomalies in the uppermost mantle is anisotropy. As the incident *P* waves that we used to calculate RF travel almost vertically below the receiver, the *P* wave and P-to-S conversions are polarized in different directions (vertical and horizontal, respectively). Consequently, if they correspond to faster and slower directions, this could cause an artificially low velocity layer [*Hacker and Abers*, 2012]. All the ray paths came from the WNW and ESE, i.e., almost normal to the trench, and parallel to the fast direction inferred by *Wagner and Long* [2013]. Therefore, anisotropy cannot explain the slow velocity in the mantle wedge.

The more likely source for such low shear velocity is the presence of melt. The relationship between the melt percent, the pore geometry, and seismic velocities at seismic frequencies is complex and poorly constrained, but melt should have a significant effect [*Abers et al*., 2014; *Hammond and Humphreys*, 2000; *McCarthy and Takei*, 2011; *Takei*, 2002]. In northeast Japan, *Nakajima et al*. [2005] observe up to 6% V_S and V_P anomalies, which are on the order of what we observe. Using the theoretical framework developed by *Takei* [2002] they explain this velocity drop by thermal effect plus 1–2% volume melt. These value seem reasonable compared to recent results from numerical modeling that predict locally up to 16% melt fraction at ~50 km depth [*Wilson et al*., 2014], i.e., where we observe a velocity reduction below Mount Rainier.

Several processes have been proposed to explain partial melting in the mantle wedge: hydration (flux) melting triggered by the fluids expelled from the slab [*Tatsumi*, 1989], melting of the downgoing sediments and/or basaltic crust [*Hsui et al*., 1983], or decompression melting due to upwelling flow [*Conder et al*., 2002]. Several authors argue that this last mechanism dominates in Cascadia based on the geometry of slow anomalies [*Gao and Shen*, 2014] and the geochemistry of volcanic products [*Leeman et al*., 2005]. All stations of Group II (gray, Figure 1) have velocities reaching values expected for melt-free peridotites at depths exceeding ~60–70 km (Figures 6–8 and 11), which gives an approximate estimate of the depth of substantial in situ melt. This depth is ~10 km shallower than the estimated top of the slab [*McGary et al*., 2014]. This could indicate that the main source of the melt is not the slab sediments or basaltic crust, although melt is likely to accumulate higher than the depths of original dehydration as the mantle is fluxed. The slow mantle velocities do not extend east of Mount Rainier (Group I), indicating that the region of melt production and/or accumulation is limited. This seems to indicate little contribution from decompression melting, which predicts the melt migrates and accumulates in a zone wider than the arc with substantial accumulation in the backarc along upwelling limbs [*Iwamori*, 2007]. This pattern also strongly reinforces the notion that an abrupt lateral thermal transition exists, immediately trenchward of arc fronts, between near-adiabatic subarc mantle and a cold forearc nose [e.g., *Syracuse et al*., 2010]; observations here suggest that the boundary can be detected within a few kilometers of the arc front. Therefore, the most likely source of melt is flux melting, largely migrating upward. This agrees with the recent observation of a vertical conductive body (resistivity under 10 Ohm/m) imaged below Mount Rainier from 5 km depth down to the top of the slab at 80 km by *McGary et al*. [2014].

7. Conclusions

We combined receiver functions and surface wave phase velocity dispersion constraints, using a transdimensional Bayesian inversion that solves for a minimum number of layers, to resolve velocity models of the crust and mantle wedge below and near Mount Rainier. This approach provides clear constraints on major interfaces along with absolute velocities above and below them, greatly aiding in interpreting composition from seismic data.

Based on their distinctive properties, the resulting models fall into two categories. Stations east of the arc have comparatively slower crust and faster mantle. Stations in the Ancestral Cascades arc, under and west of the modern arc, have faster crust and slower mantle, yielding a weak Moho signature.

By comparing our velocity profiles with theoretical seismic velocities calculated based on the local geology and globally exposed magmatic arcs, we conclude that the lower crust in the arc ranges from intermediate to felsic. We propose that intermediate-felsic to felsic rocks represent the prearc basement, indicating that the mafic Siletzia Terrane does not underlie the arc. Intermediate composition may indicate an andesitic crustal magmatic system plus solidified intrusion along the volcanic conduits. Lower-crustal velocities observed east of the arc most likely represent subduction mélanges.

The low velocities observed in the mantle wedge below the arc are best explained by the presence of melt. Because of the geometry of the inferred melting region, the most likely mechanism for magma production is flux melting within the mantle released by slab dehydration, and its upward migration. This is geographically coincident with a high conductivity region that emanates from the top of the slab.

Acknowledgments
Data were downloaded from IRIS Data Management Center (http://www.iris.edu/ds/nodes/dmc/). T. Bodin for his precious help to write and debug the codes used in this work, T. Sisson for his help to link our models to the geology of Mount Rainier and surrounding area, B. Hacker for help with Perple_X and the underlying petrology, M. Behn for his compilation of arc rock properties, and two anonymous reviewers for helping clarify several aspects of this paper. This project is funded by NSF grant EAR-1015016.

References

Abers, G. A., L. S. MacKenzie, S. Rondenay, Z. Zhang, A. G. Wech, and K. C. Creager (2009), Imaging the source region of Cascadia tremor and intermediate-depth earthquakes, *Geology*, *37*(12), 1119–1122.

Abers, G. A., K. M. Fischer, G. Hirth, D. A. Wiens, T. Plank, B. K. Holtzman, C. McCarthy, and E. Gazel (2014), Reconciling mantle attenuation-temperature relationships from seismology, petrology, and laboratory measurements, *Geochem. Geophys. Geosyst.*, *15*, 3521–3542, doi:10.1002/2014GC005444.

Aki, K. (1957), Space and time spectra of stationary waves with special reference to microtremors, *Bull. Earthquake Res. Inst. Univ. Tokyo*, *35*, 415–456.

Annen, C., J. D. Blundy, and R. S. J. Sparks (2006), The genesis of intermediate and silicic magmas in deep crustal hot zones, *J. Petrol.*, *47*(3), 505–539.

Behn, M. D., and P. B. Kelemen (2006), Stability of arc lower crust: Insights from the Talkeetna arc section, south central Alaska, and the seismic structure of modern arcs, *J. Geophys. Res.*, *111*, B11207, doi:10.1029/2006JB004327.

Bensen, G. D., M. H. Ritzwoller, M. P. Barmin, A. L. Levshin, F. Lin, M. P. Moschetti, N. M. Shapiro, and Y. Yang (2007), Processing seismic ambient noise data to obtain reliable broad-band surface wave dispersion measurements, *Geophys. J. Int.*, *169*(3), 1239–1260.

Blackwell, D. D., J. L. Steele, S. Kelley, and M. A. Korosec (1990), Heat flow in the state of Washington and thermal conditions in the Cascade Range, *J. Geophys. Res.*, *95*(B12), 19,495–19,516.

Bodin, T., M. Sambridge, H. Tkalčić, P. Arroucau, K. Gallagher, and N. Rawlinson (2012), Transdimensional inversion of receiver functions and surface wave dispersion, *J. Geophys. Res.*, *117*, B02301, doi:10.1029/2011JB008560.

Brenguier, F., N. M. Shapiro, M. Campillo, A. Nercessian, and V. Ferrazzini (2007), 3-D surface wave tomography of the Piton de la Fournaise volcano using seismic noise correlations, *Geophys. Res. Lett.*, *34*, L02305, doi:10.1029/2006GL028586.

Calkins, J. A., G. A. Abers, G. Ekström, K. C. Creager, and S. Rondenay (2011), Shallow structure of the Cascadia subduction zone beneath western Washington from spectral ambient noise correlation, *J. Geophys. Res.*, *116*, B07302, doi:10.1029/2010JB007657.

Calvert, A. J., S. L. Klemperer, N. Takahashi, and B. C. Kerr (2008), Three-dimensional crustal structure of the Mariana island arc from seismic tomography, *J. Geophys. Res.*, *113*, B01406, doi:10.1029/2007JB004939.

Conder, J. A., D. A. Wiens, and J. Morris (2002), On the decompression melting structure at volcanic arcs and back-arc spreading centers, *Geophys. Res. Lett.*, *29*(15), 1727, doi:10.1029/2002GL015390.

Connolly, J. (2005), Computation of phase equilibria by linear programming: A tool for geodynamic modeling and its application to subduction zone decarbonation, *Earth Planet. Sci. Lett.*, *236*(1), 524–541.

Couch, R. W., and R. P. Riddihough (1989), The crustal structure of the western continental margin of North America, *Geophys. Framework Cont. U.S.*, *172*, 103–128.

Currie, C., K. Wang, R. D. Hyndman, and J. He (2004), The thermal effects of steady-state slab-driven mantle flow above a subducting plate: The Cascadia subduction zone and backarc, *Earth Planet. Sci. Lett.*, *223*(1), 35–48.

du Bray, E. A., C. R. Bacon, D. A. John, J. L. Wooden, and F. K. Mazdab (2011), Episodic intrusion, internal differentiation, and hydrothermal alteration of the Miocene Tatoosh intrusive suite south of Mount Rainier, Washington, *Geol. Soc. Am. Bull.*, *123*(3–4), 534–561.

Dziewonski, A., S. Bloch, and M. Landisman (1969), A technique for the analysis of transient seismic signals, *Bull. Seismol. Soc. Am.*, *59*(1), 427–444.

Egbert, G. D., and J. R. Booker (1993), Imaging crustal structure in southwestern Washington with small magnetometer arrays, *J. Geophys. Res.*, *98*(B9), 15,967–15,985.

Ekström, G., G. A. Abers, and S. C. Webb (2009), Determination of surface-wave phase velocities across USArray from noise and Aki's spectral formulation, *Geophys. Res. Lett.*, *36*, L18301, doi:10.1029/2009GL039131.

Finn, C. (1990), Geophysical constraints on Washington convergent margin structure, *J. Geophys. Res.*, *95*(B12), 19,533–19,546.

Foster, A., G. Ekström, and M. Nettles (2014), Surface wave phase velocities of the Western United States from a two-station method, *Geophys. J. Int.*, *196*(2), 1189–1206.

Gao, H., and Y. Shen (2014), Upper mantle structure of the Cascades from full-wave ambient noise tomography: Evidence for 3D mantle upwelling in the back-arc, *Earth Planet. Sci. Lett.*, *390*, 222–233.

Gao, H., E. D. Humphreys, H. Yao, and R. D. van der Hilst (2011), Crust and lithosphere structure of the northwestern US with ambient noise tomography: Terrane accretion and Cascade arc development, *Earth Planet. Sci. Lett.*, *304*(1), 202–211.

Hacker, B. R., and G. A. Abers (2004), Subduction Factory 3: An Excel worksheet and macro for calculating the densities, seismic wave speeds, and H_2O contents of minerals and rocks at pressure and temperature, *Geochem. Geophys. Geosyst.*, *5*, Q01005, doi:10.1029/2003GC000614.

Hacker, B. R., and G. A. Abers (2012), Subduction Factory 5: Unusually low Poisson's ratios in subduction zones from elastic anisotropy of peridotite, *J. Geophys. Res.*, *117*, B06308, doi:10. /2012JB009187.

Hacker, B. R., G. A. Abers, and S. M. Peacock (2003), Subduction factory 1. Theoretical mineralogy, densities, seismic wave speeds, and H_2O contents, *J. Geophys. Res.*, *108*(B1), 2029, doi:10.1029/2001JB001127.

Hammond, W. C., and E. D. Humphreys (2000), Upper mantle seismic wave velocity: Effects of realistic partial melt geometries, *J. Geophys. Res.*, *105*(B5), 10,975–10,986.

Hildreth, W. (2007), Quaternary magmatism in the Cascades-geologic perspectives, *U.S. Geol. Surv. Prof. Pap.*, *1744*, 1–125.

Hill, G. J., T. G. Caldwell, W. Heise, D. G. Chertkoff, H. M. Bibby, M. K. Burgess, J. P. Cull, and R. A. Cas (2009), Distribution of melt beneath Mount St Helens and Mount Adams inferred from magnetotelluric data, *Nat. Geosci.*, *2*(11), 785–789.

Hsui, A. T., B. D. Marsh, and M. N. Toksöz (1983), On melting of the subducted oceanic crust: Effects of subduction induced mantle flow, *Tectonophysics*, *99*(2), 207–220.

Iwamori, H. (2007), Transportation of H_2O beneath the Japan arcs and its implications for global water circulation, *Chem. Geol.*, *239*(3), 182–198.

Jackson, I., and U. H. Faul (2010), Grainsize-sensitive viscoelastic relaxation in olivine: Towards a robust laboratory-based model for seismological application, *Phys. Earth Planet. Inter.*, *183*(1), 151–163.

Jagoutz, O., and M. D. Behn (2013), Foundering of lower island-arc crust as an explanation for the origin of the continental Moho, *Nature*, *504*(7478), 131–134.
Julia, J., C. Ammon, R. Herrmann, and A. M. Correig (2000), Joint inversion of receiver function and surface wave dispersion observations, *Geophys. J. Int.*, *143*(1), 99–112.
Jull, M., and P. Kelemen (2001), On the conditions for lower crustal convective instability, *J. Geophys. Res.*, *106*(B4), 6423–6446.
Kay, R. W., and S. Kay (1993), Delamination and delamination magmatism, *Tectonophysics*, *219*(1), 177–189.
Leeman, W. P., J. F. Lewis, R. C. Evarts, R. M. Conrey, and M. J. Streck (2005), Petrologic constraints on the thermal structure of the Cascades arc, *J. Volcanol. Geotherm. Res.*, *140*(1), 67–105.
Lees, J. M. (2007), Seismic tomography of magmatic systems, *J. Volcanol. Geotherm. Res.*, *167*(1), 37–56.
Ligorría, J. P., and C. J. Ammon (1999), Iterative deconvolution and receiver-function estimation, *Bull. Seismol. Soc. Am.*, *89*(5), 1395–1400.
Malinverno, A. (2002), Parsimonious Bayesian Markov chain Monte Carlo inversion in a nonlinear geophysical problem, *Geophys.J. Int.*, *151*(3), 675–688.
McCarthy, C., and Y. Takei (2011), Anelasticity and viscosity of partially molten rock analogue: Toward seismic detection of small quantities of melt, *Geophys. Res. Lett.*, *38*, L18306, doi:10.1029/2011GL048776.
McGary, R. S., R. L. Evans, P. E. Wannamaker, J. Elsenbeck, and S. Rondenay (2014), Pathway from subducting slab to surface for melt and fluids beneath Mount Rainier, *Nature*, *511*(7509), 338–340.
Miller, R. B. (1989), The Mesozoic Rimrock Lake inlier, southern Washington Cascades: Implications for the basement to the Columbia Embayment, *Geol. Soc. Am. Bull.*, *101*(10), 1289–1305.
Moran, S. C., J. M. Lees, and S. D. Malone (1999), P wave crustal velocity structure in the greater Mount Rainier area from local earthquake tomography, *J. Geophys. Res.*, *104*(B5), 10,775–10,786.
Nakajima, J., Y. Takei and A. Hasegawa (2005), Quantitative analysis of the inclined low-velocity zone in the mantle wedge of northeastern Japan: A systematic change of melt-filled pore shapes with depth and its implications for melt migration, *Earth Planet. Sci. Lett.*, *234*(1), 59–70.
Nichols, M., S. Malone, S. Moran, W. Thelen, and J. Vidale (2011), Deep long-period earthquakes beneath Washington and Oregon volcanoes, *J. Volcanol. Geotherm. Res.*, *200*(3), 116–128.
Ohno, I., K. Harada, and C. Yoshitomi (2006), Temperature variation of elastic constants of quartz across the alpha-beta transition, *Phys. Chem. Miner.*, *33*(1), 1–9.
Okubo, P. G., H. M. Benz, and B. A. Chouet (1997), Imaging the crustal magma sources beneath Mauna Loa and Kilauea volcanoes, Hawaii, *Geology*, *25*(10), 867–870.
Parsons, T., R. E. Wells, M. A. Fisher, E. Flueh, and U. S. Ten Brink (1999), Three-dimensional velocity structure of Siletzia and other accreted terranes in the Cascadia forearc of Washington, *J. Geophys. Res.*, *104*(B8), 18,015–18,039.
Reiners, P. W., P. E. Hammond, J. M. McKenna, and R. A. Duncan (2000), Young basalts of the central Washington Cascades, flux melting of the mantle, and trace element signatures of primary arc magmas, *Contrib. Mineral. Petrol.*, *138*(3), 249–264.
Rosenthal, J. S. (2000), Parallel computing and Monte Carlo algorithms, *Far East J. Theor. Stat.*, *4*(2), 207–236.
Rudnick, R. L., and D. M. Fountain (1995), Nature and composition of the continental crust: A lower crustal perspective, *Rev. Geophys.*, *33*(3), 267–309.
Ruprecht, P., and T. Plank (2013), Feeding andesitic eruptions with a high-speed connection from the mantle, *Nature*, *500*(7460), 68–72.
Schmandt, B., and E. Humphreys (2011), Seismically imaged relict slab from the 55 Ma Siletzia accretion to the northwest United States, *Geology*, *39*(2), 175–178.
Schmidt, M. E., A. L. Grunder, and M. C. Rowe (2008), Segmentation of the Cascade Arc as indicated by Sr and Nd isotopic variation among diverse primitive basalts, *Earth Planet. Sci. Lett.*, *266*(1), 166–181.
Shapiro, N. M., and M. Campillo (2004), Emergence of broadband Rayleigh waves from correlations of the ambient seismic noise, *Geophys. Res. Lett.*, *31*, L07614, doi:10.1029/2004GL019491.
Shen, W., M. H. Ritzwoller, V. Schulte-Pelkum, and F.-C. Lin (2013a), Joint inversion of surface wave dispersion and receiver functions: A Bayesian Monte-Carlo approach, *Geophys. J. Int.*, *192*(2), 807–836.
Shen, W., M. H. Ritzwoller, and V. Schulte-Pelkum (2013b), A 3-D model of the crust and uppermost mantle beneath the Central and Western US by joint inversion of receiver functions and surface wave dispersion, *J. Geophys. Res. Solid Earth*, *118*, 262–276, doi:10.1029/2012JB009602.
Sisson, T., V. Salters, and P. Larson (2014), Petrogenesis of Mount Rainier andesite: Magma flux and geologic controls on the contrasting differentiation styles at stratovolcanoes of the southern Washington Cascades, *Geol. Soc. Am. Bull.*, *126*(1–2), 122–144.
Stanley, W., W. Gwilliam, G. Latham, and K. Westhusing (1992), The Southern Washington Cascades conductor—A previously unrecognized thick sedimentary sequence?, *AAPG Bull.*, *76*(10), 1569–1585.
Syracuse, E. M., P. E. van Keken, and G. A. Abers (2010), The global range of subduction zone thermal models, *Phys. Earth Planet. Inter.*, *183*, 73–90, doi:10.1016/j.pepi.2010.1002.1004.
Takei, Y. (2002), Effect of pore geometry on V_p/V_s: From equilibrium geometry to crack, *J. Geophys. Res.*, *107*(B2), doi:10.1029/2001JB000522.
Tatsumi, Y. (1989), Migration of fluid phases and genesis of basalt magmas in subduction zones, *J. Geophys. Res.*, *94*(B4), 4697–4707.
Tatsumi, Y., H. Shukuno, K. Tani, N. Takahashi, S. Kodaira, and T. Kogiso (2008), Structure and growth off the Izu-Bonin-Mariana arc crust: 2. Role of crust-mantle transformation and the transparent Moho in arc crust evolution, *J. Geophys. Res.*, *113*, B02203, doi:10.1029/2007JB005121.
Wagner, L. S., and M. D. Long (2013), Distinctive upper mantle anisotropy beneath the High Lava Plains and Eastern Snake River Plain, Pacific Northwest, USA, *Geochem. Geophys. Geosyst.*, *14*, 4647–4666, doi:10.1002/ggge.20275.
Wilson, C. R., M. Spiegelman, P. E. van Keken, and B. R. Hacker (2014), Fluid flow in subduction zones: The role of solid rheology and compaction pressure, *Earth Planet. Sci. Lett.*, *401*, 261–274.
Yardley, B. W. D., and J. W. Valley (1997), The petrologic case for a dry lower crust, *J. Geophys. Res.*, *102*(B6), 12,173–12,185.